ROYAL SOCIETY
OF CHEMISTRY

## PAPER

Check for updates

# Atomically resolved surface phases of La$_{0.8}$Sr$_{0.2}$MnO$_3$(110) thin films†

Giada Franceschi, [ID] Michael Schmid, [ID] Ulrike Diebold [ID] and Michele Riva [ID] *

The atomic-scale properties of lanthanum–strontium manganite (La$_{1-x}$Sr$_x$MnO$_{3-\delta}$, LSMO) surfaces are of high interest because of the roles of the material as a prototypical complex oxide, in the fabrication of spintronic devices and in catalytic applications. This work combines pulsed laser deposition (PLD) with atomically resolved scanning tunneling microscopy (STM) and surface analysis techniques (low-energy electron diffraction – LEED, X-ray photoelectron spectroscopy – XPS, and low-energy He$^+$ ion scattering – LEIS) to assess the atomic properties of La$_{0.8}$Sr$_{0.2}$MnO$_3$(110) surfaces and their dependence on the surface composition. Epitaxial films with 130 nm thickness were grown on Nb-doped SrTiO$_3$(110) and their near-surface stoichiometry was adjusted by depositing La and Mn in sub-monolayer amounts, quantified with a movable quartz-crystal microbalance. The resulting surfaces were equilibrated at 700 °C under 0.2 mbar O$_2$, *i.e.*, under conditions that bridge the gap between ultra-high vacuum and the operating conditions of high-temperature solid-oxide fuel cells, where LSMO is used as the cathode. The atomic details of various composition-related surface phases have been unveiled. The phases are characterized by distinct structural and electronic properties and vary in their ability to accommodate deposited cations.

## Introduction

Lanthanum–strontium manganite (La$_{1-x}$Sr$_x$MnO$_{3-\delta}$, or LSMO) is a complex transition metal oxide with exciting promise for diverse technological applications. Its excellent thermal stability, carrier mobility, and redox abilities, as well as its widespread availability and environmental friendliness have appointed LSMO as the prototypical cathode material for solid-oxide fuel cells[1,2] and as a viable and cheap catalyst for methane combustion and NO oxidation.[3–6] Because of its half metallicity and colossal magnetoresistance, LSMO is also employed in spintronic applications.[7–11] Last but not least, the subtle interactions of spin, charge, orbital and lattice degrees of freedom of LSMO produce a rich phase diagram including doping- and thickness-dependent metal-to-insulator transitions, as well as (anti)ferromagnetic-to-paramagnetic transitions,[12–14] which can be exploited to achieve new functionalities in well-controlled thin-film heterostructures grown by pulsed laser deposition (PLD).[13,15]

The surface properties of LSMO are crucial in all these areas: it is at surfaces that the most relevant reactions, processes, and interactions that largely drive applications take place. For instance, high-temperature solid-oxide fuel cells are limited by the efficiency of O$_2$ activation at the surface of LSMO.[2] This and other surface reactions are affected by a complex interplay of effects that include: (i) crystallographic orientation and surface morphology;[16–20] (ii) grain and twin boundaries;[21,22] (iii) interaction with water and other gases;[23,24] (iv) surface composition, which may be affected by exsolution of Sr-rich phases;[25–30] (v) electronic properties, such as the relative alignment of the band structures of surface species and reactants,[31–36] and the oxidation state of Mn,[6,37] which is in turn tied to both the A-site doping (*i.e.*, the La/Sr ratio)[38–40] and the oxygen content;[41–43] (vi) point defects such as oxygen vacancies;[44] and (vii) the coordination chemistry of the surface species, as suggested by recent studies on the simpler relative of LSMO, SrTiO$_3$.[45] Only by disentangling the above effects can one unravel and ultimately govern the relevant processes occurring at the surface of LSMO.

To this end, it is essential to obtain a precise control over, and knowledge of, the geometric and electronic structure of LSMO surfaces and of their composition, supported by appropriate theoretical modeling. However, the nature and role of the surface structures of LSMO are to date virtually unexplored, both experimentally and computationally. With rare exceptions,[46] this extends to most quaternary oxides. Because of the lack of experimental input on the surface structures, processes occurring at the surfaces of multi-element oxides like LSMO are most often modeled based on bulk terminations.[3] However, this is a crude oversimplification of reality: the many available surface science studies on binary oxides and pioneering studies on ternary oxides[47–54] have demonstrated that their surfaces rarely show a bulk termination. Instead, they tend to exhibit

*Institute of Applied Physics, TU Wien, Wiedner Hauptstraße 8-10/E134, 1040 Wien, Austria. E-mail: riva@iap.tuwien.ac.at*

† Electronic supplementary information (ESI) available. See DOI: 10.1039/d0ta07032g

This journal is © The Royal Society of Chemistry 2020

*J. Mater. Chem. A*, 2020, **8**, 22947–22961 | **22947**

a variety of reconstructions with remarkable structural and electronic variability as a function of oxygen content and cation stoichiometry. Their building blocks consist of face-, edge-, or corner-sharing (truncated) octahedra and tetrahedra.[48,50,55–58] Their arrangement and bonding, as well as the concentration of point defects at the surface, vary strongly depending on the surface composition and on the environmental conditions, and will consequently affect the surface chemistry of the material.[45,56,59] Moving to quaternary oxides like LSMO, the complexity is only expected to increase, and so does the need to understand how the surface composition affects the surface atomic properties of the material.

The first step is to obtain reliable experimental data. To this end, one can employ the same surface science approach that has been successfully applied to unveil the surface structures of simpler binary and ternary oxides.[55–57] This approach relies on single-crystalline samples with well-defined physical properties and atomically controlled surfaces, which are explored in ultra-high vacuum (UHV). When single crystals are not readily available, as it is the case for LSMO, bulk-like epitaxial thin films offer a sound alternative. However, growing multi-element films that are thicker than a few nanometers and display the desired stoichiometry as well as the smooth surfaces required for atomic-scale investigations has proven to be challenging. In the case of LSMO, the film morphology—along with its composition, and transport and magnetic properties—was shown to depend heavily on the growth conditions,[60–66] and atomically flat surfaces were achieved only after finely tuning the growth parameters.[60,62,67,68] Even then, the attempts of imaging LSMO surfaces at the atomic scale have been unsuccessful, possibly because of the widely reported segregation of SrO at LSMO surfaces,[69–71] although some authors have also blamed charge delocalization.[68,72]

This work unveils for the first time the atomic-scale details of LSMO(110) model surfaces, relying on well-defined LSMO(110) films grown by PLD on UHV-prepared $SrTiO_3$(110) substrates.[73] In the past, both the (001) and (110) orientations of $SrTiO_3$ have been used for growing LSMO.[61,62,68,72,74] The (110) LSMO/$SrTiO_3$ interface is particularly attractive, as it lacks the polar discontinuity present at the (001) interface, and it has been hailed as a model system for investigating coupling and charge transfer in transition-metal-oxide heterostructures.[7,63,75] Atomically flat, single-crystalline films of $\approx 100$ nm thickness and $La_{0.8}Sr_{0.2}MnO_3$ composition (of interest for solid-oxide fuel cells)[2] were obtained after optimizing the PLD parameters. This work discusses the atomic-scale details of the surfaces of these films, focusing on the surface reconstructions that are stable at elevated temperatures (700 °C) and $O_2$ pressures (0.2 mbar), and on their dependence on the surface cation composition. Note that these values of pressure are well beyond what is normally used for UHV investigations, and bridge the gap between UHV and the operating conditions of LSMO-based solid-oxide electrolyzer/fuel cells (the chemical potential of oxygen at the temperature and $O_2$ pressure used in this work amounts to $\mu_O = -1.42$ eV,[76] and is very close to the one found in high-temperature solid-oxide fuel cells; e.g., $\mu_O = -1.40$ eV at 900 °C and 200 mbar $O_2$). Notably, despite the relatively harsh conditions and in contrast to other reports, no segregation of Sr-rich phases is observed. The experiments were conducted in a UHV setup combining PLD with scanning tunneling microscopy (STM), low-energy electron diffraction (LEED), X-ray photoelectron spectroscopy (XPS), and low-energy ion scattering (LEIS). The analysis has revealed that LSMO(110) displays several composition-related reconstructions, which can be reproducibly prepared and reversibly transformed by depositing sub-monolayer amounts of Mn or La from the corresponding oxidic targets (followed by equilibrating in $O_2$). Quantitative relationships between the reconstructions were established by using a movable quartz-crystal microbalance (QCM)[77] specifically designed for this purpose. The reconstructions are characterized by distinct structural, compositional, and electronic properties, and vary in their ability to accommodate the deposited cations.

Fig. 1 shows the bulk structure of the $La_{0.8}Sr_{0.2}MnO_3$ system explored in this work. Fig. 1(a) shows a 3D representation of the bulk structure of LSMO. The structure is rhombohedral $[a_R = 5.4732(2)$ Å, $\alpha_R = 60.5120(2)°]$,[78] but can be viewed as pseudocubic, i.e., a distorted version of the ideal cubic symmetry, with lattice parameter $a_{pc} = 7.7702(2)$ Å, and angle between lattice vectors of 90.4420(2)° [only half of the unit cell along (001) is shown in Fig. 1(a)].[79] Crystallographic directions given in this work are based on this pseudocubic lattice. The skeleton is built by perovskite "cubes" with sides $a = a_{pc}/2 = 3.8851(1)$ Å hosting A



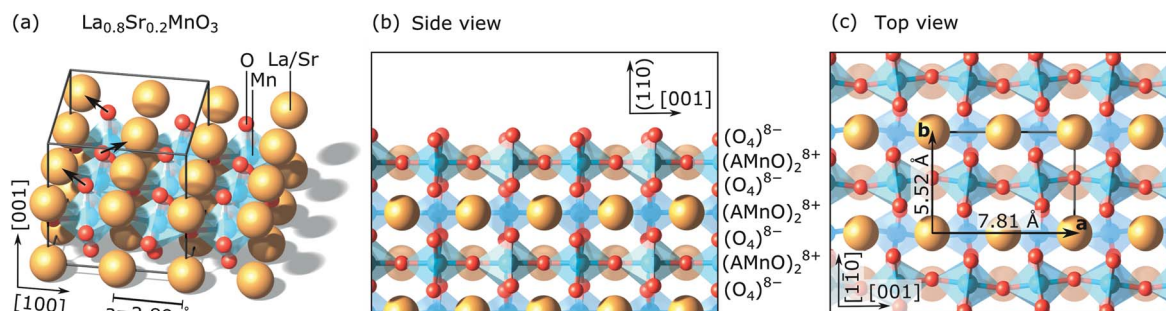Fig. 1  Bulk structure of $La_{0.8}Sr_{0.2}MnO_3$. (a) Perspective view of the bulk-truncated (001) orientation of $La_{0.8}Sr_{0.2}MnO_3$. The pseudocubic unit cell is outlined in grey. (b and c) Side and top views of the bulk-truncated (110) orientation. The direction perpendicular to the (110) surface in panel (b) is given in round brackets because there is no integer-index vector perpendicular to (110) planes. In panel (c), the lengths reported for vectors **a** and **b** assume a pseudomorphic relationship between the LSMO(110) films and the $SrTiO_3$(110) substrate. These values are used throughout the text.

22948 | J. Mater. Chem. A, 2020, 8, 22947–22961

This journal is © The Royal Society of Chemistry 2020

cations (Sr or La) at the corners and octahedrally coordinated Mn (B site) in the center. Differently from the ideal cubic perovskite, the octahedra are slightly rotated and tilted in alternating directions [see black arrows in Fig. 1(a) for the tilt], resulting in a periodicity twice as large as that of the unit cell of the ideal cubic system along $\langle 001 \rangle$. The side and top views of bulk-truncated LSMO(110) surfaces, of interest in this work, are shown in Fig. 1(b and c), respectively. The side view shows that LSMO(110) is polar, having planes of opposite charge ($\pm 8e$ per bulk unit cell assuming fully ionic species) alternating along the direction perpendicular to (110) planes. The top view highlights the (110) surface unit cell: it is twice as long in the [001] direction as the unit cell of a cubic perovskite, and identified by unit vectors **a** and **b** along [001] and [1$\bar{1}$0], respectively.

# Experimental

### Experimental apparatus

The LSMO films were grown in a UHV PLD setup (base pressure below $1 \times 10^{-10}$ mbar after bake-out) fitted for high-pressure and high-temperature growth experiments (up to 1200 °C, 1 mbar while performing reflection high-energy electron diffraction—RHEED).[80] The PLD chamber is equipped with a doubly differentially pumped TorrRHEED gun (STAIB Instruments GmbH, 35 keV beam energy), used to monitor RHEED oscillations during growth. The substrate is heated by using a collimated continuous-wave infrared laser directed on the back of the sample through a hole in the sample plate. High-purity $O_2$ (6N, further purified with an SAES purifier) is dosed via a leak valve. The PLD chamber is attached via a small transfer chamber to a surface science system (base pressure below $5 \times 10^{-11}$ mbar) with facilities for STM (SPECS Aarhus 150 used in constant-current mode, and measuring empty states, i.e., positive sample bias $U$), LEED (Omicron), XPS (non-monochromatic dual-anode Mg/Al Kα source, SPECS Phoibos 100 analyzer, normal emission), and LEIS (1 keV He$^+$, $\approx 1.5$ nA mm$^{-2}$, 132° scattering angle, 42° incidence angle; SPECS IQE 12/38, beam monochromatized with a Wien filter).

### LEIS data

LEIS is an extremely surface sensitive analysis technique: it provides information about the composition of the very topmost layers of the sample.[25] Since LEIS induces a gentle, albeit unpredictable sputtering of the surface as well as ion-beam-induced mixing, the sample was re-prepared after each LEIS acquisition by means of one cycle of sputtering−annealing, plus deposition of appropriate amounts of Mn (followed by $O_2$ annealing) to restore the original reconstruction (as judged by LEED and STM). Each LEIS spectrum shown in this work corresponds to the average of 20 consecutive scans with a total acquisition time of 10 min. Peak intensities from LEIS spectra were evaluated after subtraction of linear backgrounds. The peak area ratios obtained from the measured peak intensities do not include corrections due to different scattering cross sections or neutralization probabilities. Because of the challenges in background subtraction in LEIS spectra of metal oxides as a result of reionization,[81] absolute values should be taken with caution.

### XPS/Auger data

The intensities and positions of the Al-Kα-excited XPS peaks were evaluated with CasaXPS after subtraction of a Shirley-type background. For the evaluation of core-level shifts and Auger parameters, peak positions were obtained by fitting Gaussian–Lorentzian [GL(30)] line shapes to Mn 3s, O 1s, and Mn $L_3M_{23}M_{45}$ spectra; an asymmetric line shape [LA(1.9, 3.2, 60)] was used for Mn $2p_{3/2}$. Errors in the peak positions were derived by the automated Monte Carlo procedure available in CasaXPS, combined with linear error propagation, and multiplied by a factor of 2 to represent 95% confidence intervals.

### STM acquisition

The STM images were always acquired at room temperature, in constant-current mode, and measuring empty states (positive sample bias $U$). Electrochemically etched W tips were prepared by indentation in the film and/or by applying voltage pulses. STM images were then acquired after moving to a different spot on the sample.

### Film growth

The optimized films were grown from an LSMO target (see below for details) on SrTiO$_3$(110) single crystals, at 700 °C under an $O_2$ pressure of $4.2 \times 10^{-2}$ mbar, with 1 Hz repetition frequency, a laser fluence of 2.2 J cm$^{-2}$, and a spot size of 1.22 mm$^2$. After film growth, the temperature and $O_2$ pressure were maintained for 10 min to anneal the sample. The film thickness, estimated from RHEED oscillations, was about 130 nm. The surface composition of the films was adjusted by PLD deposition of controlled amounts of La and Mn from La$_2$O$_3$ and MnO targets, respectively [unless otherwise specified, always at room temperature (RT), at 0.2 mbar $O_2$, with a laser fluence of 1.8 J cm$^{-2}$ and 2 Hz repetition frequency, followed by $\geq 45$ min post-annealing at 700 °C, 0.2 mbar $O_2$, and ramp down 60 °C min$^{-1}$ while keeping the same $O_2$ pressure]. The doses were calibrated via deposition on a movable QCM crystal, specifically designed for this purpose as described in ref. 77. Before growth, the same area of the target that was later used for the growth was pre-ablated at the growth conditions (i.e., at the same pressure and fluence) by raster-scanning the target in the UV laser beam so that each spot was hit at least 10 times. During pre-ablation, the sample was kept in an adjoining chamber to avoid unintended deposition of material. The as-received SrTiO$_3$(110) substrates (CrysTec GmbH, 0.5 wt% Nb$_2$O$_5$-doped, $5 \times 5 \times 0.5$ mm$^3$, one-side polished, and miscut <0.3°) were cleaned and mounted as discussed elsewhere.[73] They were prepared in UHV to exhibit a mixed (4 × 1) and (5 × 1) surface reconstruction[73] (checked with STM and LEED; cleanliness always checked with XPS prior to the LSMO growth). The results presented here were quantitatively reproduced on several (>5) LSMO(110) films.

### PLD targets

The LSMO target was home-prepared, aiming to obtain better purity than commercially available products (99.9%). Appropriate amounts of lanthanum oxide (99.999%,

This journal is © The Royal Society of Chemistry 2020

J. Mater. Chem. A, 2020, **8**, 22947–22961 | **22949**

Sigma-Aldrich), strontium carbonate (99.995%, Sigma-Aldrich), and manganese(II) acetate tetrahydrate (99.999%, Alfa Aesar) were thoroughly mixed in an agate mortar, pyrolyzed in a Pt crucible, and ground to a fine powder in an agate mortar. After calcination (1 h, 1000 °C in air), the powder was isostatically pressed at RT in a hydraulic press (400 MPa; 4.3 g of powder for a cylindrical silicone mold of 16 mm inner diameter, 6 mm height, and 2 mm wall thickness), and then sintered in an alumina-tube furnace (1 h, 1450 °C, ramp rate 3 °C min$^{-1}$, and flowing $O_2$ atmosphere – 99.995% pure; the pellet was hosted inside a Pt crucible, completely embedded in non-pressed powder, and protected by a Pt lid). The target was mounted with UHV-compatible epoxy on the target holder, and then polished with SiC abrasive paper and $n$-octane (water-free solvent—the target was also re-polished before any new deposition). The target was phase pure as judged by X-ray diffraction (XRD, not shown), with 98.3% of the ideal density (buoyancy measurements), and with 99.996% purity, as measured by inductively coupled-plasma mass-spectrometry (ICP-MS); its composition was slightly A-site deficient [$(La_{0.79}Sr_{0.21})_{0.96}MnO_3$, ICP-MS], consistent with the amounts of the precursor powders used. Similar procedures and tools were employed to synthesize the MnO target. The MnO powder (3.2 g, 99.99% purity, Alfa Aesar) was isostatically pressed, and then sintered for 2 h at 1250 °C in a $N_2 : Ar = 24 : 76$ mixture. XRD (not shown) revealed the phase to be 95% MnO, plus 5% $Mn_3O_4$. The mass density was 87.9% of the theoretical density of MnO. The target was polished with SiC paper and ultrapure water, and mounted similarly to the LSMO target. La was deposited from a commercial $La_2O_3$ target (China Rare Metal Material Co., Ltd.; nominal purity better than 99.99%). Due to its high sensitivity to water, this target was always stored in UHV, and polished with water-free solvents only.

## Results

Aiming to shed light on the surface atomic properties of LSMO(110) and on how they depend on the surface cation stoichiometry, sub-monolayer amounts of Mn and La were deposited on atomically flat and stoichiometric LSMO(110) films from MnO and $La_2O_3$ targets followed by high-pressure annealing ($\geq$45 min,
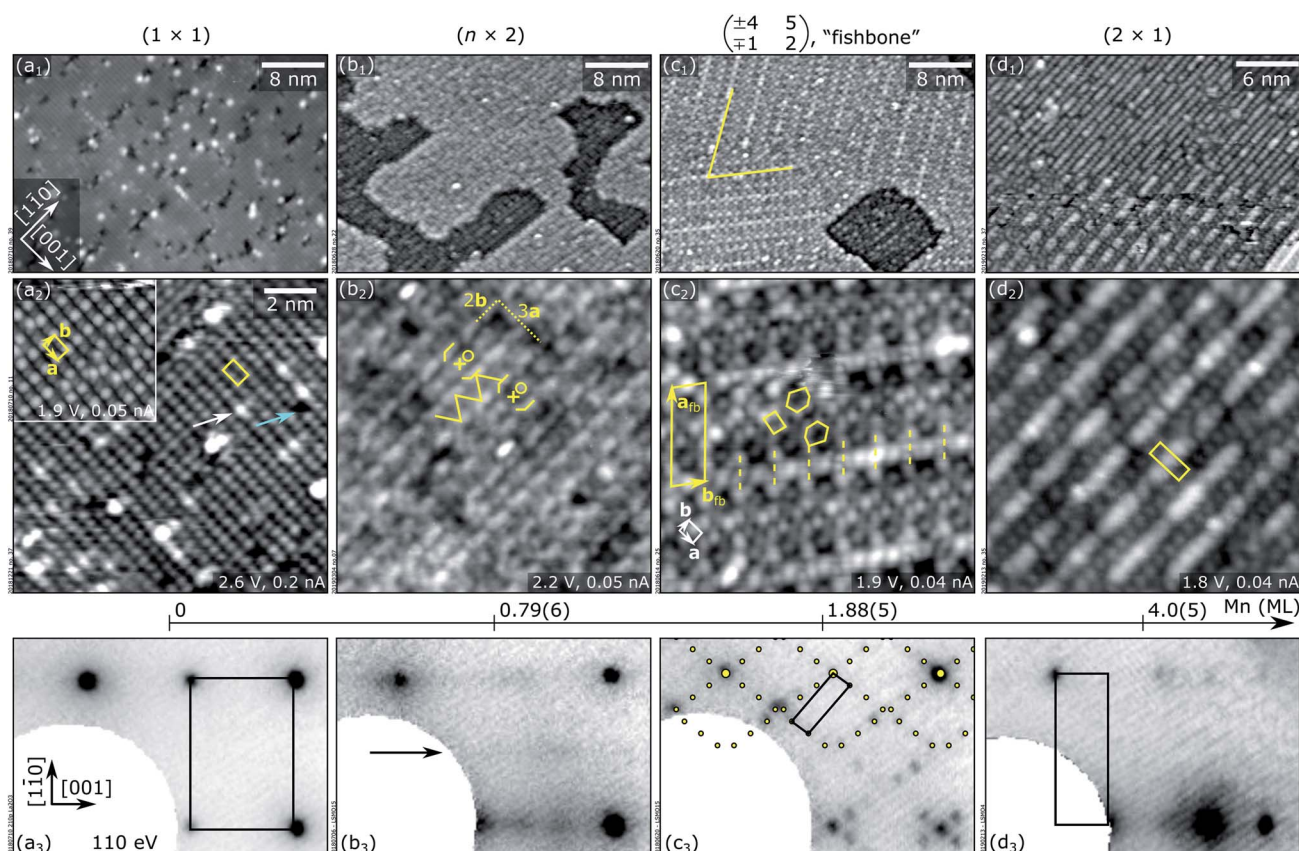


Fig. 2 Surface phase diagram of $La_{0.8}Sr_{0.2}MnO_3$(110) as a function of near-surface stoichiometry. The stable surface reconstructions of LSMO(110) are shown as they appear in STM (top row, 40 × 28 nm$^2$; middle row, 12 × 12 nm$^2$) and LEED (bottom row). The reconstructions have been obtained by depositing sub-monolayer amounts of La or Mn on atomically flat LSMO(110) films at RT, followed by $O_2$ annealing at 700 °C, 0.2 mbar for 1 h. The bottom axis reports the relative doses of Mn cations (uncertainties are indicated in parentheses), which were established as detailed further below. One monolayer (ML) is defined as the number of Mn sites in an $(AMnO)_2$ plane of LSMO(110), i.e., 4.64 × 10$^{14}$ cm$^{-2}$. The (1 × 1) surface in panel (a$_2$) and the (2 × 1) surface in panel (d$_1$) are shown with two different STM tip terminations. The unit cells are highlighted in the close-up images and in the LEED patterns. Enlarged versions of the atomic-scale STM images are shown in Section S1.†

**22950** | J. Mater. Chem. A, 2020, **8**, 22947–22961

This journal is © The Royal Society of Chemistry 2020

700 °C, and 0.2 mbar $O_2$, see the Experimental section). At each deposition step, the corresponding changes were studied with STM, LEED, XPS, and LEIS. It is worth mentioning that the evolution of the surface structures has not been investigated systematically as a function of the Sr content (see the Discussion for more comments on this point). Fig. 2 summarizes the stable surface reconstructions of LSMO(110) that have been identified with this approach, as seen in atomically resolved STM images (top and middle rows) and in the corresponding LEED patterns (bottom row). The reconstructions are displayed as a function of cation composition (bottom axis), which has been established as detailed below. Deposition of Mn and La with PLD is the most reliable method to select a specific surface termination among those shown in the phase diagram, but it is not the only one: $Ar^+$ sputtering (plus $O_2$ annealing) removes Mn (and oxygen) preferentially over A-site species, and can thus also be used to move towards the left-hand side of the phase diagram. It is likely that the preferential removal of Mn by $Ar^+$ is a consequence of preferential sputtering of oxygen that is a well-established effect on oxides:[82] among the undercoordinated cations left behind, Mn and Sr preferentially re-evaporate over La because of their higher vapor pressure,[83] and Mn is preferentially removed over Sr because of the higher oxygen affinity of Sr.

The following analysis identifies the characteristic building blocks of each structure and discusses their geometric arrangement and periodicity, setting the stage for building the corresponding structural models in the future. Note that, because STM images contain both topographic and electronic information, it is generally not straightforward to provide a one-to-one relationship between features observed in STM and the geometric position of atoms. The following discussion proceeds from A-site rich towards B-site rich reconstructions, as achieved by depositing Mn in PLD (followed by $O_2$ annealing). If not specified otherwise, the same qualitative observations hold true when moving in the opposite direction by depositing La (or by $Ar^+$ sputtering), and the transitions between the reconstructions are reversible.

### (1 × 1)

The $(1 \times 1)$ structure is the leftmost (*i.e.*, most A-site rich) reconstruction of the phase diagram in Fig. 2. It reproduces the periodicity of the bulk-truncated LSMO(110), *i.e.*, a cell twice as long in the [001] direction as the unit cell of a cubic perovskite oxide. The $(1 \times 1)$ periodicity is apparent from both the LEED pattern of Fig. 2($a_3$) and the STM images of Fig. 2($a_2$). The rectangular unit cell [yellow in Fig. 2($a_2$), $7.8 \times 5.5$ Å$^2$] is defined by the unit vectors **a** and **b** running along the [001] and the [1$\bar{1}$0] directions, respectively. STM shows two common appearances of the surface, as achieved with two distinct (yet unknown) tip terminations. Two protrusions per unit cell are always observed [corresponding to one protrusion per (110) unit cell of a cubic perovskite], with a corrugation of $\approx 25$ pm across the [001]-oriented rows. Depending on the tip termination, all protrusions may appear identical [main ($a_2$) panel], or every other feature along the [001] direction may appear brighter (inset). A few defects (the number depends on the preparation conditions) are present,

as indicated by the cyan and white arrows in Fig. 2($a_2$). They are imaged as dark and bright features at the lattice positions.

Deposition of Mn causes a phase separation of the surface: discrete patches of the $(n \times 2)$ superstructure of Fig. 2($b_1$) form and coexist with the remaining, structurally unchanged $(1 \times 1)$ areas. With more Mn deposited, the $(n \times 2)$ patches become more numerous and grow in size. Depending on the tunneling conditions and on the tip termination, the apparent height of the $(1 \times 1)$ phase may appear as either higher or lower than that of $(n \times 2)$, suggesting that the apparent contrast is most likely of electronic origin.

### (n × 2)

The $(n \times 2)$ structure is poorly ordered, and is characterized by a large number of structural defects. However, a few building blocks can be identified. Lines of "boomerang" features [marked by yellow "J"-shaped lines in Fig. 2($b_2$)] run along the [1$\bar{1}$0] direction. These boomerangs are separated from one another by 2**b**. This two-fold periodicity along [1$\bar{1}$0] is also visible in the LEED pattern of Fig. 2($b_3$) as a faint horizontal line (highlighted by an arrow) midway between integer-order spots. Two boomerangs, mirrored by a [1$\bar{1}$0] line, enclose two sites marked by circles and "+" symbols in Fig. 2($b_2$). These sites may appear as depressions, or they may be occupied by a single, bright dot, or by a feature elongated along the [001] direction. The entities consisting of two boomerangs and the enclosed features are referred to as "blocks". Two orientations of the blocks, mirrored by a [001] line, are generally present on the surface [Fig. 2($b_2$) shows only one of them]. Adjacent lines of blocks are separated by $n = 2$, 3, or 5 lattice units along **a**, and can be stacked in phase (*i.e.*, with no shift along [1$\bar{1}$0]), or can be shifted by one **b** lattice vector. "Linker" structures connecting adjacent rows of blocks correspondingly appear aligned along [001], or as a zig-zag line, as outlined in Fig. 2($b_2$). The large variety of possible combinations within the $(n \times 2)$ surface (internal structure of blocks, spacing between adjacent lines along both in-plane directions) is the cause for the poor order of the structure. This is also reflected in the LEED pattern of Fig. 2($b_3$), which shows an increased intensity along the [001] direction in-between integer-order spots rather than well-defined maxima. As a consequence, a single well-defined unit cell cannot be identified.

The $(n \times 2)$ reconstruction can only be prepared in mono-phase form when La is deposited starting from the "fishbone" reconstruction of Fig. 2($c_1$). When depositing Mn on a $(1 \times 1)$-reconstructed surface, small, disconnected patches of $(n \times 2)$ initially form that coexist with the remaining $(1 \times 1)$ areas, but, upon further deposition, they do not grow big enough to fill the whole surface: they soon transform into the fishbone reconstruction described below, such that $(1 \times 1)$ and fishbone areas coexist. This hysteretic behavior suggests that the $(n \times 2)$ reconstruction may be a metastable phase.

### Fishbone

The periodicity of the so-called "fishbone" surface can be derived from the LEED pattern in Fig. 2($c_3$), overlaid with its simulated pattern.[84] It can be expressed in matrix notation as
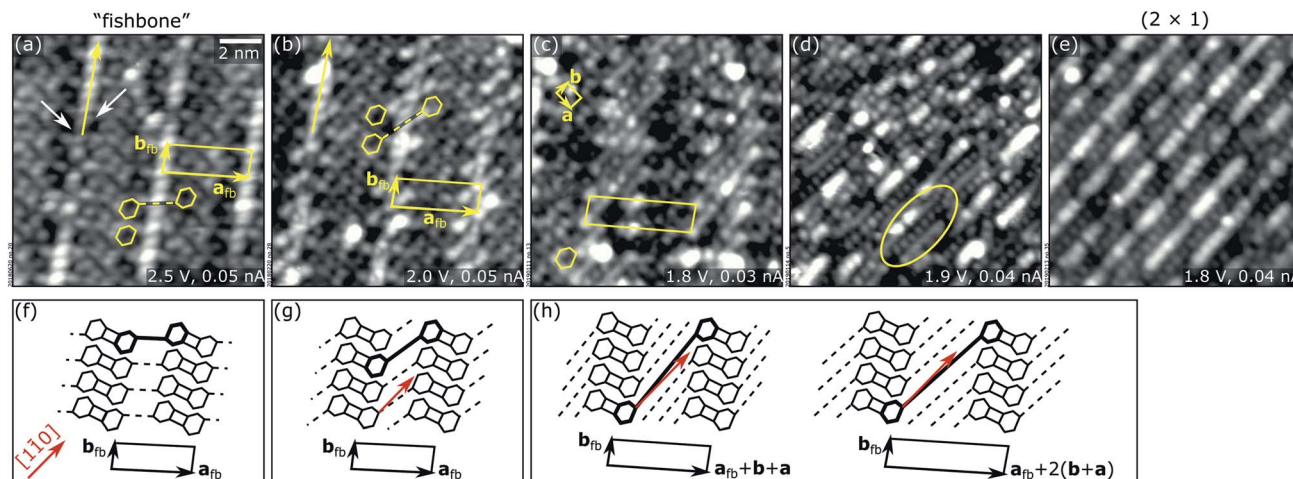
This journal is © The Royal Society of Chemistry 2020

*J. Mater. Chem. A*, 2020, **8**, 22947–22961 | **22951**

Fig. 3 Transition from "fishbone" to $(2 \times 1)$. (a–e) $12 \times 12$ nm$^2$ STM images revealing a continuous transition from the "fishbone" to the $(2 \times 1)$ reconstruction with increasing Mn concentration. (f–h) Sketches of the main structural changes during the transition from panel (a) to panel (c). Red arrows in (g and h) are oriented along [1$\bar{1}$0]. The rotation of the dashed connecting lines in panel (g) with respect to the [1$\bar{1}$0] direction is $\approx 10°$. By depositing more Mn, the superstructure periodicities change from $\mathbf{a}_{fb} = \pm 4\mathbf{a} + 5\mathbf{b}$ [panels (a, b) and (f, g)] to $\mathbf{a}_{fb} + n(\mathbf{b} \pm \mathbf{a})$, with $n = 1$ at moderate Mn doses, and $n = 2$ at larger deposited amounts (the two signs correspond to the two mirror-symmetric domains). These periodicities are indicated in the sketches of panel (h). The angles between the [1$\bar{1}$0] direction and the dashed lines connecting rings in panel (h) are $\approx 4.5°$ and $\approx 4°$ for $n = 1, 2$, respectively.

$$\begin{pmatrix} \mathbf{a}_{fb} \\ \mathbf{b}_{fb} \end{pmatrix} = \begin{pmatrix} -4 & 5 \\ 1 & 2 \end{pmatrix} \begin{pmatrix} \mathbf{a} \\ \mathbf{b} \end{pmatrix}$$

where the vectors $\mathbf{a}$, $\mathbf{b}$, and $\mathbf{a}_{fb}$, $\mathbf{b}_{fb}$ identify the unit cell of the $(1 \times 1)$ reconstruction and of the 13-times bigger unit cell of the fishbone, respectively [see the close-up STM image in Fig. 2(c$_2$)]. Because the angle between $\mathbf{a}_{fb}$ and $\mathbf{b}_{fb}$ is different than the one between $\mathbf{a}$ and $\mathbf{b}$, it is not possible to express this periodicity in Wood's notation. Two mirror domains contribute to the complex LEED pattern, as seen in Fig. 2(c$_1$) (the superlattice matrix of the second domain can be obtained by changing the sign of either column). The details of one of these domains are shown in Fig. 2(c$_2$), where bright rows parallel to $\mathbf{b}_{fb}$ are visible, crossed by short lines parallel to $\mathbf{a}_{fb}$ (dashed yellow lines). Between two adjacent $\mathbf{b}_{fb}$ rows, two sets of six-membered rings can be seen (outlined in yellow). In the $\mathbf{b}_{fb}$ direction, these sets are shifted with respect to each other by $b_{fb}/2$, and rotated in plane by $180°$. One of the vertices of each ring coincides with the endpoint of a short line parallel to $\mathbf{a}_{fb}$ (dashed). The closest four vertices of two neighboring rings form a rectangle [also highlighted in yellow in Fig. 2(c$_1$)] that has the shape and dimensions of a $(1 \times 1)$ unit cell, albeit rotated by $\approx 10°$.

Fig. 3 illustrates the transition between the fishbone and the $(2 \times 1)$ structure. The transition is continuous and without any phase separation, exposing different reconstructions with common structural building blocks. In Fig. 3, STM images of the structures (top row) are accompanied by the corresponding sketches (bottom row).

For small Mn doses [Fig. 3(b and g)], minor changes are observed in the initial fishbone structure of Fig. 3(a and f). The structure has the same shape and size of the unit cell, and retains the main features of the fishbone, i.e., bright ridges (long, yellow arrows along $\mathbf{b}_{fb}$) and rows of rings along $\mathbf{b}_{fb}$ coupled by rectangles.

The only difference is in the structures that connect the rings with each other across the bright ridges. In the structure of Fig. 3(b), two additional features are introduced at the positions indicated by the white arrows in Fig. 3(a). This causes an apparent rotation towards [1$\bar{1}$0] of the "connection lines" (dashed) between the rings, now connecting next-nearest-neighbor rings rather than nearest neighbors [compare the sketches in Fig. 3(f) and (g)].

Further deposition of Mn [see Fig. 3(c and h)] increases the spatial periodicity of the superstructure and produces longer connecting lines (now appearing as either continuous or dotted) that again exhibit different rotation angles close to the [1$\bar{1}$0] direction [see sketches in Fig. 3(h) and caption]. Two structures with different periodicities, shown in the sketches of Fig. 3(h), tend to coexist at the surface, the one with larger periodicity being predominant on Mn-richer surfaces. As a result of the many possible shifts required to create the two coexisting superstructures, the surface appears increasingly disordered in this regime as the Mn dose increases. Eventually the rings disappear [see Fig. 3(d)], and the connecting lines locally appear as alternating dotted and continuous lines [oval in Fig. 3(d)], parallel to, or slightly rotated with respect to [1$\bar{1}$0]. Finally, small, bright features appear on top of the continuous line, which grow longer with more Mn deposited, until the $(2 \times 1)$ surface of Fig. 3(e) is formed. As the structures of Fig. 3 tend to coexist at the surface rather than forming monophase phases, determining the corresponding Mn coverages is not trivial.

## $(2 \times 1)$

The periodicity of the $(2 \times 1)$ surface is seen in LEED [Fig. 2(d$_3$)] and in STM images acquired at high bias voltages [empty sample states, above 1.8 V, see Fig. 2(d$_2$)]. The structure consists
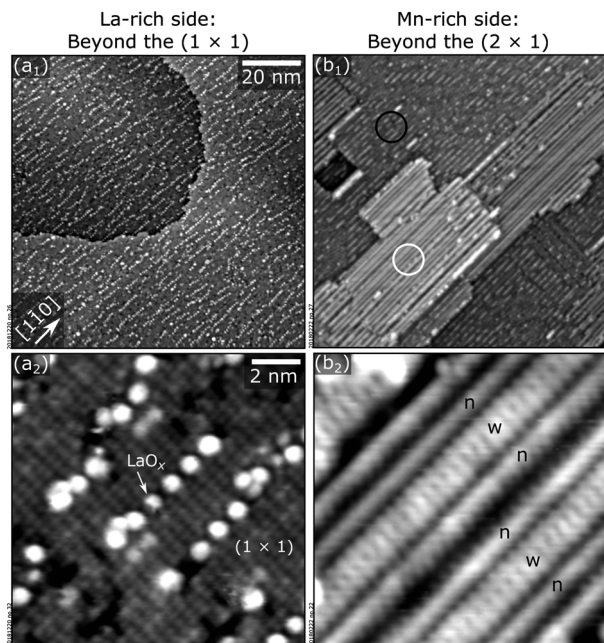
22952 | J. Mater. Chem. A, 2020, 8, 22947–22961

This journal is © The Royal Society of Chemistry 2020

La-rich side:
Beyond the (1 × 1)

Mn-rich side:
Beyond the (2 × 1)

**Fig. 4** La-rich and Mn-rich surface structures beyond the phase diagram of Fig. 2. ($a_1$ and $a_2$) $100 \times 100$ nm$^2$ and $12 \times 12$ nm$^2$ STM images ($U = 2$ V, $I_t = 0.2$ nA) of a surface of LSMO(110) La-richer than the (1 × 1) reconstruction. The periodicity of the (1 × 1) surface is largely preserved, but additional bright features aligned along the [1$\bar{1}$0] direction appear. ($b_1$ and $b_2$) STM images (again $100 \times 100$ nm$^2$ and $12 \times 12$ nm$^2$) of surfaces Mn-richer than the (2 × 1) surface structure. While the majority of the surface (black circle) retains the (2 × 1) reconstruction, some patches (white circle) exhibit bright lines as in the $12 \times 12$ nm$^2$ STM image of panel ($b_2$).

of dotted lines with an alternating apparent height, all oriented along the [1$\bar{1}$0] direction. The brighter lines (larger apparent height) appear fragmented, and shifts by **b**/2 can be present in the whole structure. Notice that at low bias voltages the surface commonly appears as in the top part of the STM image of Fig. 2($d_1$), where both lines show a similar apparent height—a tip change made the bottom part of Fig. 2($d_1$) appear as in Fig. 2($d_2$). This suggests that the difference in the apparent height observed at high bias voltages has significant electronic contributions.

Further deposition of Mn starting from a (2 × 1)-reconstructed surface results in other structures not included in the phase diagram of Fig. 2 [see Fig. 4(b)]. It is worth mentioning the challenges in preparing a monophase sample with the (2 × 1) reconstruction: at times, limited patches of the surface reconstruction described in Fig. 4(b) were observed before realizing the monophase (2 × 1). This difficulty is possibly due to kinetic limitations at the conditions used during post-deposition annealing.

**Beyond the phase diagram of Fig. 2**

Fig. 4 shows LSMO(110) surfaces that are richer in La or Mn [panels (a) and (b), respectively] than those reported in the phase diagram of Fig. 2. Deposition of La on the (1 × 1) surface [Fig. 2(a)] induces the formation of [1$\bar{1}$0]-oriented chains of protrusions with a typical separation of 2**b**, appearing white in the STM images of Fig. 4(a). Depending on the tunneling conditions and/or the tip termination, the chains can also be imaged as depressions (not shown). The (1 × 1) structure is otherwise preserved. Because the A-site signal in XPS and LEIS is higher than on (1 × 1)-reconstructed surfaces (not shown), it is reasonable to assume that the bright protrusions correspond to (La,Sr)O$_x$ complexes. Such features can also be obtained with sufficiently long Ar$^+$ sputtering (followed by O$_2$ annealing) starting from any of the structures shown in Fig. 2 (the Mn-richer the initial structure, the longer the sputtering time required).

Fig. 4(b) reports instead the typical morphology observed upon deposition of Mn on the (2 × 1) surface of Fig. 2(d). The majority of the surface preserves the (2 × 1) appearance [black circle in Fig. 4($b_1$)], but patches of a new structure are formed [white circle in Fig. 4($b_1$); close-up image in Fig. 4($b_2$)]. The new ($m \times 1$) structure consists of bright lines of different widths and separations, all oriented along the [1$\bar{1}$0] direction. For small doses of Mn, narrow lines such as those labeled by "n" in Fig. 4($b_2$) form and patch together. As the Mn dose increases, wider lines ["w" in Fig. 4($b_2$)] are also formed, which tend to be sandwiched by the narrow lines in a narrow–wide–narrow arrangement. As the amount of Mn increases further, this reconstruction covers an increasingly larger fraction of the surface, at the expense of the (2 × 1) areas. However,
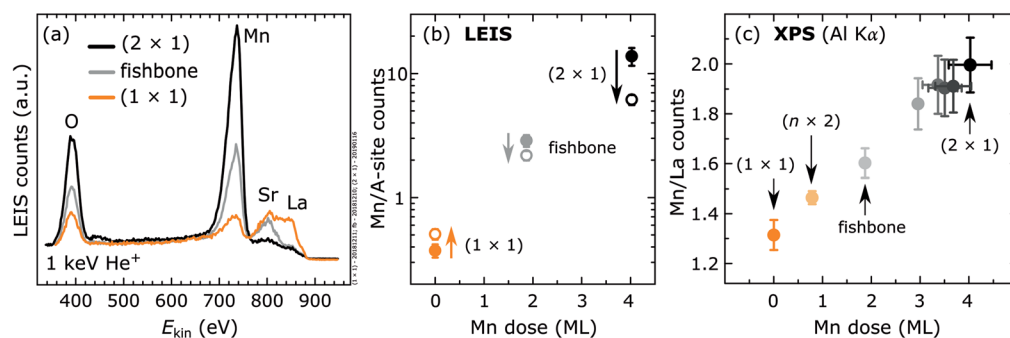


**Fig. 5** Relative compositions of the LSMO(110) surface structures. (a) LEIS spectra of the (1 × 1) (orange), fishbone (grey), and (2 × 1) (black) structures. (b) Mn-to-A-site area ratios from LEIS. Full circles: values extracted from the spectra in panel (a). Open circles: subsequent acquisition. Arrows show the change of the ratio caused by the slight sputtering/mixing induced by the LEIS He$^+$ beam. (c) Mn 2p-to-La 4d peak area ratios from XPS.

This journal is © The Royal Society of Chemistry 2020

*J. Mater. Chem. A*, 2020, **8**, 22947–22961 | **22953**

a monophase sample with this ($m \times 1$) superstructure was never observed, likely because deposited Mn species stick less on Mn-richer surfaces, as is elucidated in Section S2.†

### Relative compositions

As one moves along the phase diagram (deposition of Mn or La plus $O_2$ annealing), the reconstructions appear increasingly Mn-richer from the left- to the right-hand side of Fig. 2, both from LEIS [Fig. 5(a and b)] and from the analysis of the intensity of XPS core-level peaks [Fig. 5(c) – sample spectra are provided in Fig. S4†]. Thanks to the sufficiently large compositional differences, both techniques allow one to identify any given surface reconstruction. On the other hand, the La 4d/Sr 3d XPS intensity ratios are identical (within the error bars) for all the phases of Fig. 2, and no apparent trend in the La-to-Sr ratio is visible from the available LEIS spectra.

In LEIS, the Mn-to-A-site area ratios on ($1 \times 1$)- and ($2 \times 1$)-reconstructed surfaces differ by more than one order of magnitude, while the changes in the XPS signal are less dramatic [Fig. 5(b and c)]. This indicates that the Mn-rich surfaces have their Mn mainly in their top-most layers, while the layers below (still within the probing depth of XPS) are closer to an $AMnO_3$ stoichiometry. This notion is supported by prolonged LEIS acquisition. Fig. 5(b) compares two sets of consecutive acquisitions on each reconstruction (each acquisition corresponds to the average of 20 consecutive spectra; full and open circles correspond to the first and the second acquisition, respectively). The Mn signal decreases over time on the fishbone and on the ($2 \times 1$) structures. This is because $He^+$ ions cause a mild sputtering and intermixing in the near-surface region (roughly 10 nm according to a SRIM[85] calculation), preferentially removing the abundant surface Mn species from the very surface. In contrast, the Mn signal of the ($1 \times 1$) surface increases over time, possibly because Mn species are less abundant at the top surface layer (if at all present), and Mn atoms in the subsurface are made accessible with longer LEIS acquisition as a result of the mild sputtering/mixing. This

behavior suggests that the ($1 \times 1$) phase belongs to another family with respect to the other structures of the phase diagram of Fig. 2.

The bottom axes of Fig. 2 and 5(b and c) show the relative composition of the surface structures in terms of monolayers (ML) of Mn cations. As discussed in more detail in Section S2 of the ESI,† this calibration has been achieved by:

(i) Evaluating the number of laser pulses to be shot on the MnO target to move between adjacent reconstructions. Notice that this evidenced pronounced differences among the different surface phases of LSMO(110) in the sticking/re-evaporation probability of the deposited species. The effective amounts of material needed to move between the reconstructions were evaluated by accounting for these effects.

(ii) Obtaining the growth rate of Mn atoms under the given conditions. This has been achieved by means of a specially designed QCM:[77] incremental amounts of manganese oxide were deposited on the QCM from the MnO target, and the corresponding mass growth rate was derived from a linear fit of the data. After deriving the composition of the deposited film with XPS ($MnO_2$), a growth rate of $(1.97 \pm 0.03) \times 10^{-2}$ ML of Mn per pulse was derived.

(iii) Translating the effective number of pulses shot on the MnO target (i) into ML of Mn, by using the growth rate from (ii).

### Electronic properties

To gain insights into the electronic properties of the surface phases of LSMO(110) presented in this work, the distance between Mn $2p_{3/2}$ and O 1s core level positions and the Mn($2p_{3/2}$, $L_3M_{23}M_{45}$) Auger parameter were evaluated as a function of surface composition. These two quantities, shown in Fig. 6(a and b), respectively, yield information about the oxidation state of Mn species at the surface, and about the character of the metal–oxygen bonding among the different surface phases of Fig. 2.

Most commonly, the oxidation state of Mn in Mn-containing compounds is determined based on the shape of
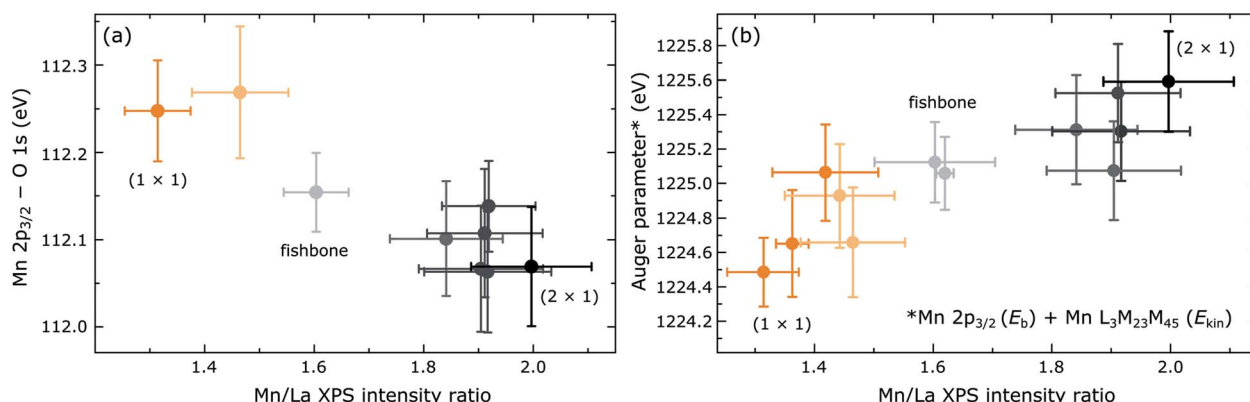


**Fig. 6** (a) Mn $2p_{3/2}$ − O 1s core-level binding energy differences as a function of surface stoichiometry. The trend is consistent with a change in the oxidation state of the Mn species at the surface. (b) Mn($2p_{3/2}$, $L_3M_{23}M_{45}$) Auger parameters of the different reconstructions of LSMO(110) films as a function of surface stoichiometry. The trend is interpreted in terms of a change in the character of the metal–oxygen bonds at the surface, increasingly covalent (and/or decreasing bandgap) as the Mn coverage increases.

**22954** | *J. Mater. Chem. A*, 2020, **8**, 22947–22961

This journal is © The Royal Society of Chemistry 2020

a few relevant peaks (see Section S2†). This was not possible in the present work, due to (i) the overlap of Mn 3s with Al K$\alpha_{3,4}$-induced La 4d satellites, (ii) the rather large full-width at half-maximum of the Mn 2p peaks [see Fig. S4(b)†], and (iii) the low surface sensitivity due to the normal-emission configuration (grazing exit was precluded by the geometrical constraints of the apparatus). Instead, the distance between Mn $2p_{3/2}$ and O 1s peaks was used for this purpose. Since this quantity does not depend on band shifts with respect to the Fermi level,[86] it is a good metric to gain information about the Mn oxidation state. The values for reference manganese oxide compounds in Table S1† show a clear decreasing trend of the distance between Mn $2p_{3/2}$ and O 1s peaks with decreasing Mn oxidation state (i.e., increasing Mn content in the reference compound). A consistent trend is visible in Fig. 6(a), suggesting that Mn-richer surface phases of LSMO(110) are associated with lower Mn oxidation states. However, because the XPS signals are dominated by bulk contributions (normal emission setup, inelastic mean free path of $\approx 2$ nm), the shifts measured are much smaller than those that would originate from the surface layers alone, and one cannot pinpoint the absolute values of the oxidation state of Mn atoms at the surface. The fact that a difference is even at all observed is a strong indication that the different reconstructions are characterized by different Mn oxidation states. Notice that the absolute value of the shifts in Fig. 6(a) would indicate the oxidation state expected for bulk LSMO, i.e., between +3 and +4 (cf. Table S1†), consistently with the fact that the XPS signals are dominated by bulk contributions.

The Mn($2p_{3/2}$, $L_3M_{23}M_{45}$) Auger parameter in Fig. 6(b) shows an approximately linear increase with increasing Mn enrichment at the surface. Auger parameters are calculated as the sum of the energy positions of a core level peak (expressed in binding energy) and an Auger peak (expressed in kinetic energy), and they effectively describe the extent to which photo-induced core holes are screened by ligands (O) surrounding the ionized atom (Mn) and by conduction-band electrons (resulting from the ionization of cations).[87] Efficient screening is typically achieved in small-bandgap materials, where a large number of delocalized electrons are available to participate, and/or when the metal–oxygen bonds have a strong covalent character. Hence, the data in Fig. 6(b) suggest that the different phases of LSMO(110) are characterized by increasingly covalent Mn–O bonds and/or decreasing bandgaps as a function of Mn enrichment. For completeness, the Auger parameters of oxygen [O(1s, $KL_{23}L_{23}$)] and La [La($3d_{5/2}$, MNN)] were also determined (not shown). These Auger parameters do not substantially change with the Mn content at the surface. The absence of a trend in the oxygen Auger parameter is at odds with the correlation between metal and oxygen Auger parameters observed for other oxide compounds.[88]

## Discussion

### Structural, compositional, and electronic diversity

The experimental data presented here on the reconstructions of LSMO(110) testify to their remarkable structural and electronic variety as a function of surface composition. Importantly, each reconstruction can be uniquely identified by its appearance in STM and by its Mn-to-A-site content (as determined with XPS or LEIS). This level of control over the single surface phases sets the stage to isolate a few critical factors that are known/expected to affect the surface reactivity of LSMO, namely its composition,[89] the surface atomic structure (through the surface coordination chemistry),[45] the Mn oxidation state,[37] and the ionicity of the metal–oxygen bonds. Notably, because the presented phases are stable under conditions that bridge the gap between UHV and the operating conditions of high-temperature solid-oxide fuel cells, they are an ideal test bed to address the oxygen incorporation driving these devices.[45]

While presenting the appearance of the surface structures in STM, the building blocks of each structure and their geometric arrangements have been identified and discussed. Among the presented phases, the (1 × 1) structure [Fig. 2(a)] is a particularly promising and appealing candidate for *ab initio* methods. Not only does it show a comparatively simple appearance and a small-enough unit cell, it may also be the first example among complex perovskite oxides of a strongly A-site-rich reconstruction that is stable under close-to-realistic conditions. A-site-rich structures are rarely resolved in perovskite oxide surfaces,[46,90] which rather tend to consist of one or two layers of B-site cations coordinated to oxygen.[58,91] Nonetheless, the formation of A-site-rich structures is often held responsible for the deactivation of perovskite oxide surfaces in solid-oxide fuel cells.[25–30] Obtaining a structural model for an A-site rich surface such as the (1 × 1) phase would be extremely valuable to better understand this process. The A-site richness of the (1 × 1) structure is consistent with the trend of the Mn Auger parameter as a function of surface composition [Fig. 6(b)]. The comparatively small value measured on (1 × 1)-reconstructed surfaces indicates an ionic character and a large bandgap, which is expected for a surface dominated by A–O bonds. Consistently, the Mn-richer structures are characterized by an increasingly more covalent bonding environment.

Increasing the Mn content at the surface creates surface reconstructions beyond the (1 × 1) phase, and more complex structures with larger unit cells are encountered. Fig. 3 reveals that one can move between these Mn-rich reconstructions *via* a smooth transition in which common building blocks are retained and whose relative arrangement changes as a function of Mn content. Identifying these building blocks is the first step to build quantitative structural models: the identification of structural units and their relative arrangement has been crucial to solve many of the surface reconstructions formed on (001)-, (110)-, and (111)-oriented $SrTiO_3$ and related perovskite oxides.[58] Similarly to these systems, also the Mn-rich reconstructions of LSMO probably consist of variously arranged tetrahedra and octahedra. Notice that other multi-element oxides (mostly ternary) besides LSMO(110) were shown to display numerous and complex surface reconstructions depending on the cation and/or oxygen stoichiometry.[46,49,51–54,92] This suggests that the rich structural variety shown by the LSMO(110) surface may be the rule rather than the exception among multi-element oxides.

This journal is © The Royal Society of Chemistry 2020

*J. Mater. Chem. A*, 2020, **8**, 22947–22961 | **22955**

The XPS data in Fig. 6 show that the structural diversity witnessed among the surface phases of LSMO(110) is accompanied by a similar variety in their electronic properties. The trend in the binding energy difference of Mn $2p_{3/2}$ and O 1s peaks [Fig. 6(a)] suggests that Mn-richer structures are associated with lower oxidation states of Mn. The fact that these differences are present does not come as a surprise: the oxidation state of Mn in A-doped manganites such as LSMO is sensitive to the doping level[38–40] and to the oxygen chemical potential (*i.e.*, the concentration of oxygen vacancies).[41] While most generally a mixture of +3/+4 with variable ratio is measured, +2 was also observed under reducing conditions at the surface of LSMO films.[42,43] Given the relatively large compositional differences among the surface phases of LSMO(110) (see the bottom axis of Fig. 2), differences in the corresponding Mn oxidation state are to be expected.

### Origin of the surface reconstructions

As seen from Fig. 1(b), the unreconstructed LSMO crystal is polar along the (110) orientation, consisting of alternating planes with a charge of $\pm 8e$ per unit cell (taking oxidation states as charges, and neglecting the contribution of the small equilibrium concentration of oxygen vacancies at 700 °C and 0.2 mbar $O_2$, *i.e.*, $\approx 2 \times 10^{-8}$ of the O sites[93]). Without any polarity-compensating mechanism, this would result in a diverging dipole moment with increasing crystal thickness, *i.e.*, an unstable system.[94] Realizing reconstructions with appropriate net charge [$-4e$ per unit cell on top of the $(AMnO)_2$ termination; $+4e$ per unit cell above $O_4$ planes] could compensate for this polar catastrophe.[94,95] The surface reconstructions of other polar multi-element oxides, also related to one another by differences of near-surface stoichiometry, have been interpreted this way.[48,49,51,94] Generally, for the reconstructions to bear the same charge per unit cell despite a change in cation composition, the oxygen stoichiometry and/or the oxidation state of the cations must change. For example, the polarity-compensating reconstructions of $SrTiO_3$(110) are distinguished by (i) different Ti-to-O compositions, (ii) different coordination of the cations to the oxygen species,[91] and possibly (iii) slight differences in the oxidation state of Ti.[96]

There is evidence that similar mechanisms are also at play in LSMO(110): first, its reconstructions display clear compositional differences. Moreover, the trend of the binding energy difference between Mn $2p_{3/2}$ and O 1s peaks indicates differences in the Mn oxidation states. The high quality of the surfaces of these films will allow, *e.g.*, performing X-ray absorption spectroscopy to pinpoint the coordination and/or the oxidation state of the surface species in the future.[91]

### La/Sr content

The Sr doping level in LSMO is important to its performance: it defines many of the bulk properties [LSMO undergoes metal–insulator and (anti)ferromagnetic–paramagnetic transitions as a function of Sr content, and also the crystallographic structure depends on the Sr doping[14]], and can also affect surface reactivity. Particularly critical for the operation of solid-oxide fuel cells is the

widely reported segregation of Sr-rich phases under operating conditions, which tends to degrade the oxygen exchange activity at the surface.[89] Sr segregation and the formation of insulating Sr-rich clusters is a very common phenomenon observed in LSMO and other perovskite oxides under conditions comparable to those employed in this work,[26,70] and it has been widely investigated, both experimentally and theoretically.[27,89] Notably, the films presented in this work do not show this phenomenon. XPS does not indicate any substantial deviation of the La-to-Sr ratio from the nominal composition in the near-surface region. Moreover, the films neither show the expected Sr segregation nor the formation of insulating, Sr-rich clusters upon prolonged (>5 h) annealing at 700 °C and 0.2 mbar $O_2$: the A-site-to-Mn and the La-to-Sr XPS intensity ratios stay unaltered, and the surface structures appear unchanged in STM, always retaining atomically flat morphologies. It is likely that the Sr segregation observed in polycrystalline and textured films and in ceramic samples under comparable conditions is due to grain and twin boundaries that favor Sr diffusion,[97,98] which are absent in the single-crystalline films presented here. It is also possible that the epitaxial strain imposed by the $SrTiO_3$ substrate has a role in suppressing Sr segregation.[99,100]

Regarding the La/Sr ratio among the different surface phases of Fig. 2, there seems to be no evident trend as a function of Mn content. As mentioned in the Results section, the La 4d/Sr 3d XPS ratio among the surfaces of Fig. 2 appears unchanged within the error bars (*i.e.*, within $\approx 10\%$). However, this could be due to the low surface sensitivity of XPS at the high kinetic energies where the Sr 3d and La 4d peaks are found ($\approx 1350$ eV and $\approx 1380$ eV, respectively). Similarly, the La/Sr LEIS intensity ratios show a strong scatter ($\approx 50\%$ of the average) without an apparent trend, but it is hard to determine whether the measured differences are to be assigned to slightly different sample treatments. Small variations in the La/Sr ratio in LEIS have also been observed among surface structures that appear identical in STM. These differences are likely due to different sample history that can alter the near-surface composition (*e.g.*, sputtering−annealing is preferential to Sr over La). It is possible that small variations in the La/Sr ratio (with the same Mn/A-site ratio) are compensated for by introducing a small number of oxygen vacancies or by changing the oxidation state of Mn, without changing the overall appearance of the surface phase. A systematic investigation of the LSMO(110) surface as a function of Sr content, by depositing Sr or SrO, accompanied by a detailed characterization of surface point defects, would be needed for an increased understanding of the effect of the La/Sr ratio on the surface properties of LSMO(110).

## Conclusions

This work breaks new ground regarding the surface characterization of quaternary oxides, focusing on the model (110) surface of single-crystalline LSMO films. It shows that LSMO(110) exhibits several surface phases that are stable under conditions (700 °C and 0.2 mbar $O_2$) that bridge the gap between UHV and the operating conditions of high-temperature solid-oxide fuel cells where LSMO is used as the cathode. These surface phases were tuned by depositing La and Mn on atomically flat LSMO(110) films (followed by $O_2$ annealing), in

**22956** | *J. Mater. Chem. A*, 2020, **8**, 22947–22961

This journal is © The Royal Society of Chemistry 2020

amounts that were accurately quantified. A combined STM, XPS, and LEIS analysis has revealed that the surface phases differ substantially in their atomic structure, composition, and electronic properties, and that they are differently prone to accommodate deposited cations.

The abundant structural and electronic variety uncovered by this study on a model quaternary oxide surface demonstrates that the surface atomic details must be accounted for when modeling surface processes on multi-element oxides. The insights presented build the foundation for developing quantitative structural models, which are required to understand the surface phenomena driving LSMO-based devices.

## Conflicts of interest

There are no conflicts to declare.

## Acknowledgements

## References

1 C. Sun, R. Hui and J. Roller, Cathode materials for solid oxide fuel cells: a review, *J. Solid State Electrochem.*, 2010, **14**, 1125, DOI: 10.1007/s10008-009-0932-0.

2 S. P. Jiang, Development of lanthanum strontium manganite perovskite cathode materials of solid oxide fuel cells: a review, *J. Mater. Sci.*, 2008, **43**, 6799, DOI: 10.1007/s10853-008-2966-6.

3 J. Hwang, R. R. Rao, L. Giordano, Y. Katayama, Y. Yu and Y. Shao-Horn, Perovskites in catalysis and electrocatalysis, *Science*, 2017, **358**, 751, DOI: 10.1126/science.aam7092.

4 Y. Wang, H. Arandiyan, H. A. Tahini, J. Scott, X. Tan, H. Dai, J. D. Gale, A. L. Rohl, S. C. Smith and R. Amal, The controlled disassembly of mesostructured perovskites as an avenue to fabricating high performance nanohybrid catalysts, *Nat. Commun.*, 2017, **8**, 15553, DOI: 10.1038/ncomms15553.

5 C. H. Kim, G. Qi, K. Dahlberg and W. Li, Strontium-doped perovskites rival platinum catalysts for treating $NO_x$ in simulated diesel exhaust, *Science*, 2010, **327**, 1624, DOI: 10.1126/science.1184087.

6 S. Ponce, M. A. Peña and J. L. G. Fierro, Surface properties and catalytic performance in methane combustion of Sr-substituted lanthanum manganites, *Appl. Catal., B*, 2000, **24**, 193, DOI: 10.1016/S0926-3373(99)00111-3.

7 S. Majumdar and S. van Dijken, Pulsed laser deposition of $La_{1-x}Sr_xMnO_3$: thin-film properties and spintronic applications, *J. Phys. D*, 2013, **47**, 034010, DOI: 10.1088/0022-3727/47/3/034010.

8 J.-H. Park, E. Vescovo, H.-J. Kim, C. Kwon, R. Ramesh and T. Venkatesan, Direct evidence for a half-metallic ferromagnet, *Nature*, 1998, **392**, 794, DOI: 10.1038/33883.

9 Y. Tokura, Critical features of colossal magnetoresistive manganites, *Rep. Prog. Phys.*, 2006, **69**, 797, DOI: 10.1088/0034-4885/69/3/R06.

10 J. Huang, H. Wang, X. Sun, X. Zhang and H. Wang, Multifunctional $La_{0.67}Sr_{0.33}MnO_3$ (LSMO) thin films integrated on mica substrates toward flexible spintronics and electronics, *ACS Appl. Mater. Interfaces*, 2018, **10**, 42698, DOI: 10.1021/acsami.8b16626.

11 A. M. Haghiri-Gosnet, T. Arnal, R. Soulimane, M. Koubaa and J. P. Renard, Spintronics: perspectives for the half-metallic oxides, *Phys. Status Solidi A*, 2004, **201**, 1392, DOI: 10.1002/pssa.200304403.

12 J. Junquera and P. Ghosez, Critical thickness for ferroelectricity in perovskite ultrathin films, *Nature*, 2003, **422**, 506, DOI: 10.1038/nature01501.

13 Z. Liao and J. Zhang, Metal-to-insulator transition in ultrathin manganite heterostructures, *Appl. Sci.*, 2019, **9**, 144, DOI: 10.3390/app9010144.

14 J. Hemberger, A. Krimmel, T. Kurz, H.-A. Krug von Nidda, V. Y. Ivanov, A. A. Mukhin, A. M. Balbashov and A. Loidl, Structural, magnetic, and electrical properties of single-crystalline $La_{1-x}Sr_xMnO_3$ ($0.4 < x < 0.85$), *Phys. Rev. B*, 2002, **66**, 094410, DOI: 10.1103/PhysRevB.66.094410.

15 D. G. Schlom, Perspective: Oxide molecular-beam epitaxy rocks!, *APL Mater.*, 2015, **3**, 062403, DOI: 10.1063/1.4919763.

16 L. Yan, K. R. Balasubramaniam, S. Wang, H. Du and P. A. Salvador, Effects of crystallographic orientation on the oxygen exchange rate of $La_{0.7}Sr_{0.3}MnO_3$ thin films, *Solid State Ionics*, 2011, **194**, 9, DOI: 10.1016/j.ssi.2011.05.004.

17 M. Burriel, H. Téllez, R. J. Chater, R. Castaing, P. Veber, M. Zaghrioui, T. Ishihara, J. A. Kilner and J.-M. Bassat, Influence of crystal orientation and annealing on the oxygen diffusion and surface exchange of $La_2NiO_{4+\delta}$, *J. Phys. Chem. C*, 2016, **120**, 17927, DOI: 10.1021/acs.jpcc.6b05666.

18 S. H. Chang, N. Danilovic, K.-C. Chang, R. Subbaraman, A. P. Paulikas, D. D. Fong, M. J. Highland, P. M. Baldo, V. R. Stamenkovic, J. W. Freeland, J. A. Eastman and N. M. Markovic, Functional links between stability and reactivity of strontium ruthenate single crystals during oxygen evolution, *Nat. Commun.*, 2014, **5**, 4191, DOI: 10.1038/ncomms5191.

19 K. Kerman, C. Ko and S. Ramanathan, Orientation dependent oxygen exchange kinetics on single crystal $SrTiO_3$ surfaces, *Phys. Chem. Chem. Phys.*, 2012, **14**, 11953, DOI: 10.1039/C2CP41918A.

20 M. Burriel, J. Peña-Martinez, R. J. Chater, S. Fearn, A. V. Berenov, S. J. Skinner and J. A. Kilner, Anisotropic

This journal is © The Royal Society of Chemistry 2020

*J. Mater. Chem. A*, 2020, **8**, 22947–22961 | **22957**

oxygen ion diffusion in layered $PrBaCo_2O_{5+\delta}$, *Chem. Mater.*, 2012, **24**, 613, DOI: 10.1021/cm203502s.

21 R. A. De Souza and M. Martin, Probing diffusion kinetics with secondary ion mass spectrometry, *MRS Bull.*, 2009, **34**, 907, DOI: 10.1557/mrs2009.212.

22 E. Navickas, T. M. Huber, Y. Chen, W. Hetaba, G. Holzlechner, G. Rupp, M. Stöger-Pollach, G. Friedbacher, H. Hutter, B. Yildiz and J. Fleig, Fast oxygen exchange and diffusion kinetics of grain boundaries in Sr-doped $LaMnO_3$ thin films, *Phys. Chem. Chem. Phys.*, 2015, **17**, 7659, DOI: 10.1039/C4CP05421K.

23 A. Staykov, S. Fukumori, K. Yoshizawa, K. Sato, T. Ishihara and J. Kilner, Interaction of SrO-terminated $SrTiO_3$ surface with oxygen, carbon dioxide, and water, *J. Mater. Chem. A*, 2018, **6**, 22662, DOI: 10.1039/C8TA05177A.

24 J. Yang, J. M. Polfus, Z. Li, H. L. Tuller and B. Yildiz, Role of adsorbate coverage on the oxygen dissociation rate on Sr-doped $LaMnO_3$ surfaces in the presence of $H_2O$ and $CO_2$, *Chem. Mater.*, 2020, **32**, 5483, DOI: 10.1021/acs.chemmater.9b05243.

25 J. Druce, H. Téllez, M. Burriel, M. D. Sharp, L. J. Fawcett, S. N. Cook, D. S. McPhail, T. Ishihara, H. H. Brongersma and J. A. Kilner, Surface termination and subsurface restructuring of perovskite-based solid oxide electrode materials, *Energy Environ. Sci.*, 2014, **7**, 3593, DOI: 10.1039/C4EE01497A.

26 Z. Cai, M. Kubicek, J. Fleig and B. Yildiz, Chemical heterogeneities on $La_{0.6}Sr_{0.4}CoO_{3-\delta}$ thin films–correlations to cathode surface activity and stability, *Chem. Mater.*, 2012, **24**, 1116, DOI: 10.1021/cm203501u.

27 W. Lee, J. W. Han, Y. Chen, Z. Cai and B. Yildiz, Cation size mismatch and charge interactions drive dopant segregation at the surfaces of manganite perovskites, *J. Am. Chem. Soc.*, 2013, **135**, 7909, DOI: 10.1021/ja3125349.

28 Y. Chen, H. Téllez, M. Burriel, F. Yang, N. Tsvetkov, Z. Cai, D. W. McComb, J. A. Kilner and B. Yildiz, Segregated chemistry and structure on (001) and (100) surfaces of $(La_{1-x}Sr_x)_2CoO_4$ override the crystal anisotropy in oxygen exchange kinetics, *Chem. Mater.*, 2015, **27**, 5436, DOI: 10.1021/acs.chemmater.5b02292.

29 H. Téllez, J. Druce, Y.-W. Ju, J. Kilner and T. Ishihara, Surface chemistry evolution in $LnBaCo_2O_{5+\delta}$ double perovskites for oxygen electrodes, *Int. J. Hydrogen Energy*, 2014, **39**, 20856, DOI: 10.1016/j.ijhydene.2014.06.102.

30 Y. Chen, W. Jung, Z. Cai, J. J. Kim, H. L. Tuller and B. Yildiz, Impact of Sr segregation on the electronic structure and oxygen reduction activity of $SrTi_{1-x}Fe_xO_3$ surfaces, *Energy Environ. Sci.*, 2012, **5**, 7979, DOI: 10.1039/C2EE21463F.

31 Y.-L. Lee, J. Kleis, J. Rossmeisl, Y. Shao-Horn and D. Morgan, Prediction of solid oxide fuel cell cathode activity with first-principles descriptors, *Energy Environ. Sci.*, 2011, **4**, 3966, DOI: 10.1039/C1EE02032C.

32 N. A. Deskins, R. Rousseau and M. Dupuis, Defining the role of excess electrons in the surface chemistry of $TiO_2$, *J. Phys. Chem. C*, 2010, **114**, 5891, DOI: 10.1021/jp101155t.

33 M. T. Greiner, M. G. Helander, W.-M. Tang, Z.-B. Wang, J. Qiu and Z.-H. Lu, Universal energy-level alignment of

molecules on metal oxides, *Nat. Mater.*, 2012, **11**, 76, DOI: 10.1038/nmat3159.

34 M. T. Greiner, L. Chai, M. G. Helander, W.-M. Tang and Z.-H. Lu, Transition metal oxide work functions: the influence of cation oxidation state and oxygen vacancies, *Adv. Funct. Mater.*, 2012, **22**, 4557, DOI: 10.1002/adfm.201200615.

35 Y. Chen, Z. Cai, Y. Kuru, W. Ma, H. L. Tuller and B. Yildiz, Electronic activation of cathode superlattices at elevated temperatures – source of markedly accelerated oxygen reduction kinetics, *Adv. Energy Mater.*, 2013, **3**, 1221, DOI: 10.1002/aenm.201300025.

36 R. Merkle and J. Maier, Oxygen incorporation into Fe-doped $SrTiO_3$: Mechanistic interpretation of the surface reaction, *Phys. Chem. Chem. Phys.*, 2002, **4**, 4140, DOI: 10.1039/B204032H.

37 J. Chen, H. Arandiyan, X. Gao and J. Li, Recent advances in catalysts for methane combustion, *Catal. Surv. Asia*, 2015, **19**, 140, DOI: 10.1007/s10563-015-9191-5.

38 A. T. Kozakov, A. G. Kochur, K. A. Googlev, A. V. Nikolskii, V. I. Torgashev, V. G. Trotsenko and A. A. Bush, Valence state of manganese and iron ions in $La_{1-x}A_xMnO_3$ (A = Ca, Sr) and $Bi_{1-x}Sr_xFeO_3$ systems from Mn 2p, Mn 3s, Fe 2p and Fe 3s X-ray photoelectron spectra. Effect of delocalization on Fe 3s spectra splitting, *J. Alloys Compd.*, 2015, **647**, 947, DOI: 10.1016/j.jallcom.2015.06.161.

39 M. Abbate, F. M. F. de Groot, J. C. Fuggle, A. Fujimori, O. Strebel, F. Lopez, M. Domke, G. Kaindl, G. A. Sawatzky, M. Takano, Y. Takeda, H. Eisaki and S. Uchida, Controlled-valence properties of $La_{1-x}Sr_xFeO_3$ and $La_{1-x}Sr_xMnO_3$ studied by soft-X-ray absorption spectroscopy, *Phys. Rev. B*, 1992, **46**, 4511, DOI: 10.1103/PhysRevB.46.4511.

40 T. Saitoh, A. E. Bocquet, T. Mizokawa, H. Namatame, A. Fujimori, M. Abbate, Y. Takeda and M. Takano, Electronic structure of $La_{1-x}Sr_xMnO_3$ studied by photoemission and X-ray-absorption spectroscopy, *Phys. Rev. B*, 1995, **51**, 13942, DOI: 10.1103/PhysRevB.51.13942.

41 E. Beyreuther, S. Grafström, L. M. Eng, C. Thiele and K. Dörr, XPS investigation of Mn valence in lanthanum manganite thin films under variation of oxygen content, *Phys. Rev. B*, 2006, **73**, 155425, DOI: 10.1103/PhysRevB.73.155425.

42 M. P. de Jong, I. Bergenti, V. A. Dediu, M. Fahlman, M. Marsi and C. Taliani, Evidence for $Mn^{2+}$ ions at surfaces of $La_{0.7}Sr_{0.3}MnO_3$ thin films, *Phys. Rev. B.*, 2005, **71**, 014434, DOI: 10.1103/PhysRevB.71.014434.

43 K. A. Stoerzinger, M. Risch, J. Suntivich, W. M. Lü, J. Zhou, M. D. Biegalski, H. M. Christen, A. Ariando, T. Venkatesan and Y. Shao-Horn, Oxygen electrocatalysis on (001)-oriented manganese perovskite films: Mn valency and charge transfer at the nanoscale, *Energy Environ. Sci.*, 2013, **6**, 1582, DOI: 10.1039/C3EE40321A.

44 M. M. Kuklja, E. A. Kotomin, R. Merkle, Y. A. Mastrikov and J. Maier, Combined theoretical and experimental analysis of processes determining cathode performance in solid oxide fuel cells, *Phys. Chem. Chem. Phys.*, 2013, **15**, 5443, DOI: 10.1039/C3CP44363A.

22958 | *J. Mater. Chem. A*, 2020, **8**, 22947–22961

This journal is © The Royal Society of Chemistry 2020

45 M. Riva, M. Kubicek, X. Hao, G. Franceschi, S. Gerhold, M. Schmid, H. Hutter, J. Fleig, C. Franchini, B. Yildiz and U. Diebold, Influence of surface atomic structure demonstrated on oxygen incorporation mechanism at a model perovskite oxide, *Nat. Commun.*, 2018, **9**, 3710, DOI: 10.1038/s41467-018-05685-5.

46 A. Tselev, R. K. Vasudevan, A. G. Gianfrancesco, L. Qiao, P. Ganesh, T. L. Meyer, H. N. Lee, M. D. Biegalski, A. P. Baddorf and S. V. Kalinin, Surface control of epitaxial manganite films via oxygen pressure, *ACS Nano*, 2015, **9**, 4316, DOI: 10.1021/acsnano.5b00743.

47 M. Riva, G. Franceschi, M. Schmid and U. Diebold, Epitaxial growth of complex oxide films: Role of surface reconstructions, *Phys. Rev. Res.*, 2019, **1**, 033059, DOI: 10.1103/PhysRevResearch.1.033059.

48 J. A. Enterkin, A. K. Subramanian, B. C. Russell, M. R. Castell, K. R. Poeppelmeier and L. D. Marks, A homologous series of structures on the surface of $SrTiO_3$(110), *Nat. Mater.*, 2010, **9**, 245, DOI: 10.1038/nmat2636.

49 D. Kienzle, P. Koirala and L. D. Marks, Lanthanum aluminate (110) $3\times1$ surface reconstruction, *Surf. Sci.*, 2015, **633**, 60, DOI: 10.1016/j.susc.2014.11.016.

50 D. M. Kienzle, A. E. Becerra-Toledo and L. D. Marks, Vacant-site octahedral tilings on $SrTiO_3$(001), the $(\sqrt{13} \times \sqrt{13})R33.7°$ surface, and related structures, *Phys. Rev. Lett.*, 2011, **106**, 176102, DOI: 10.1103/PhysRevLett.106.176102.

51 T. K. Andersen, S. Wang, M. R. Castell, D. D. Fong and L. D. Marks, Single-layer $TiO_x$ reconstructions on $SrTiO_3$(111): $(\sqrt{7} \times \sqrt{7})R19.1°$, $(\sqrt{13} \times \sqrt{13})R13.9°$, and related structures, *Surf. Sci.*, 2018, **675**, 36, DOI: 10.1016/j.susc.2018.04.011.

52 S. Förster and W. Widdra, Growth, structure, and thermal stability of epitaxial $BaTiO_3$ films on Pt(111), *Surf. Sci.*, 2010, **604**, 2163, DOI: 10.1016/j.susc.2010.09.009.

53 A. M. Kolpak, D. Li, R. Shao, A. M. Rappe and D. A. Bonnell, Evolution of the structure and thermodynamic stability of the $BaTiO_3$(001) surface, *Phys. Rev. Lett.*, 2008, **101**, 036102, DOI: 10.1103/PhysRevLett.101.036102.

54 N. Doudin, D. Kuhness, M. Blatnik, F. P. Netzer and S. Surnev, Phase behaviour of 2D $MnWO_x$ and $FeWO_x$ ternary oxide layers on Pd(100), *J. Phys.: Condens. Matter*, 2017, **29**, 234004, DOI: 10.1088/1361-648X/aa6f3c.

55 G. S. Parkinson, Iron oxide surfaces, *Surf. Sci. Rep.*, 2016, **71**, 272, DOI: 10.1016/j.surfrep.2016.02.001.

56 D. R. Mullins, The surface chemistry of cerium oxide, *Surf. Sci. Rep.*, 2015, **70**, 42, DOI: 10.1016/j.surfrep.2014.12.001.

57 U. Diebold, The surface science of titanium dioxide, *Surf. Sci. Rep.*, 2003, **48**, 53, DOI: 10.1016/S0167-5729(02)00100-0.

58 T. K. Andersen, D. D. Fong and L. D. Marks, Pauling's rules for oxide surfaces, *Surf. Sci. Rep.*, 2018, **73**, 213, DOI: 10.1016/j.surfrep.2018.08.001.

59 Z. Jakub, J. Hulva, M. Meier, R. Bliem, F. Kraushofer, M. Setvin, M. Schmid, U. Diebold, C. Franchini and G. S. Parkinson, Local structure and coordination define adsorption in a model $Ir_1/Fe_3O_4$ single-atom catalyst,

*Angew. Chem. Int. Ed.*, 2019, **131**, 14099, DOI: 10.1002/ange.201907536.

60 H. Guo, D. Sun, W. Wang, Z. Gai, I. Kravchenko, J. Shao, L. Jiang, T. Z. Ward, P. C. Snijders, L. Yin, J. Shen and X. Xu, Growth diagram of $La_{0.7}Sr_{0.3}MnO_3$ thin films using pulsed laser deposition, *J. Appl. Phys.*, 2013, **113**, 234301, DOI: 10.1063/1.4811187.

61 E. Annese, T. J. A. Mori, P. Schio, B. Rache Salles and J. C. Cezar, Influence of the growth parameters on the electronic and magnetic properties of $La_{0.67}Sr_{0.33}MnO_3$ epitaxial thin films, *Appl. Surf. Sci.*, 2018, **437**, 281, DOI: 10.1016/j.apsusc.2017.12.164.

62 R. Bachelet, D. Pesquera, G. Herranz, F. Sánchez and J. Fontcuberta, Persistent two-dimensional growth of (110) manganite films, *Appl. Phys. Lett.*, 2010, **97**, 121904, DOI: 10.1063/1.3490713.

63 J. X. Ma, X. F. Liu, T. Lin, G. Y. Gao, J. P. Zhang, W. B. Wu, X. G. Li and J. Shi, Interface ferromagnetism in (110)-oriented $La_{0.7}Sr_{0.3}MnO_3$/$SrTiO_3$ ultrathin superlattices, *Phys. Rev. B*, 2009, **79**, 174424, DOI: 10.1103/PhysRevB.79.174424.

64 M. Huijben, L. W. Martin, Y.-H. Chu, M. B. Holcomb, P. Yu, G. Rijnders, D. H. A. Blank and R. Ramesh, Critical thickness and orbital ordering in ultrathin $La_{0.7}Sr_{0.3}MnO_3$ films, *Phys. Rev. B*, 2008, **78**, 094413, DOI: 10.1103/PhysRevB.78.094413.

65 M. Koubaa, A. M. Haghiri-Gosnet, R. Desfeux, P. Lecoeur, W. Prellier and B. Mercey, Crystallinity, surface morphology, and magnetic properties of $La_{0.7}Sr_{0.3}MnO_3$ thin films: an approach based on the laser ablation plume range models, *J. Appl. Phys.*, 2003, **93**, 5227, DOI: 10.1063/1.1566093.

66 J. Chen, M. Döbeli, D. Stender, K. Conder, A. Wokaun, C. W. Schneider and T. Lippert, Plasma interactions determine the composition in pulsed laser deposited thin films, *Appl. Phys. Lett.*, 2014, **105**, 114104, DOI: 10.1063/1.4895788.

67 A. Rana, K. Bogle, O. Game, S. Patil, N. Valanoor and S. Ogale, Nanoscale modulation of electronic states across unit cell steps on the surface of an epitaxial colossal magnetoresistance manganite film, *Appl. Phys. Lett.*, 2010, **96**, 263108, DOI: 10.1063/1.3455886.

68 H. M. Rønnow, C. Renner, G. Aeppli, T. Kimura and Y. Tokura, Polarons and confinement of electronic motion to two dimensions in a layered manganite, *Nature*, 2006, **440**, 1025, DOI: 10.1038/nature04650.

69 T. T. Fister, D. D. Fong, J. A. Eastman, P. M. Baldo, M. J. Highland, P. H. Fuoss, K. R. Balasubramaniam, J. C. Meador and P. A. Salvador, In situ characterization of strontium surface segregation in epitaxial $La_{0.7}Sr_{0.3}MnO_3$ thin films as a function of oxygen partial pressure, *Appl. Phys. Lett.*, 2008, **93**, 151904, DOI: 10.1063/1.2987731.

70 H. Jalili, Y. Chen and B. Yildiz, Structural, chemical, and electronic state on $La_{0.7}Sr_{0.3}MnO_3$ dense thin-film surfaces at high temperature: surface segregation, *ECS Trans.*, 2010, **28**, 235, DOI: 10.1149/1.3495846.

This journal is © The Royal Society of Chemistry 2020

*J. Mater. Chem. A*, 2020, **8**, 22947–22961 | **22959**

71 H. Dulli, P. A. Dowben, S.-H. Liou and E. W. Plummer, Surface segregation and restructuring of colossal-magnetoresistant manganese perovskites $La_{0.65}Sr_{0.35}MnO_3$, *Phys. Rev. B*, 2000, **62**, R14629, DOI: 10.1103/PhysRevB.62.R14629.

72 T. Becker, C. Streng, Y. Luo, V. Moshnyaga, B. Damaschke, N. Shannon and K. Samwer, Intrinsic inhomogeneities in manganite thin films investigated with scanning tunneling spectroscopy, *Phys. Rev. Lett.*, 2002, **89**, 237203, DOI: 10.1103/PhysRevLett.89.237203.

73 M. Riva, G. Franceschi, Q. Lu, M. Schmid, B. Yildiz and U. Diebold, Pushing the detection of cation nonstoichiometry to the limit, *Phys. Rev. Mater.*, 2019, **3**, 043802, DOI: 10.1103/PhysRevMaterials.3.043802.

74 P. Perna, C. Rodrigo, E. Jiménez, F. J. Teran, N. Mikuszeit, L. Méchin, J. Camarero and R. Miranda, Tailoring magnetic anisotropy in epitaxial half metallic $La_{0.7}Sr_{0.3}MnO_3$ thin films, *J. Appl. Phys.*, 2011, **110**, 013919, DOI: 10.1063/1.3605542.

75 S. Majumdar, K. Kooser, T. Elovaara, H. Huhtinen, S. Granroth and P. Paturi, Analysis of electronic structure and its effect on magnetic properties in (001) and (110) oriented $La_{0.7}Sr_{0.3}MnO_3$ thin films, *J. Phys.: Condens. Matter*, 2013, **25**, 376003, DOI: 10.1088/0953-8984/25/37/376003.

76 G. Franceschi, M. Wagner, J. Hofinger, T. Krajňák, M. Schmid, U. Diebold and M. Riva, Growth of $In_2O_3(111)$ thin films with optimized surfaces, *Phys. Rev. Mater.*, 2019, **3**, 103403, DOI: 10.1103/PhysRevMaterials.3.103403.

77 G. Franceschi, M. Schmid, U. Diebold and M. Riva, Movable holder for a quartz crystal microbalance for exact growth rates in pulsed laser deposition, *Rev. Sci. Instrum.*, 2020, **91**, 065003, DOI: 10.1063/5.0007643.

78 L. Rørmark, K. Wiik, S. Stølen and T. Grande, Oxygen stoichiometry and structural properties of $La_{1-x}A_xMnO_{3\pm\delta}$ (A = Ca or Sr and $0 \le x \le 1$), *J. Mater. Chem.*, 2002, **12**, 1058, DOI: 10.1039/b103510j.

79 H. D. Megaw and C. N. W. Darlington, Geometrical and structural relations in the rhombohedral perovskites, *Acta Crystallogr. A*, 1975, **31**, 161, DOI: 10.1107/S0567739475000332.

80 S. Gerhold, M. Riva, B. Yildiz, M. Schmid and U. Diebold, Adjusting island density and morphology of the $SrTiO_3(110)$-$(4\times1)$ surface: Pulsed laser deposition combined with scanning tunneling microscopy, *Surf. Sci.*, 2016, **651**, 76, DOI: 10.1016/j.susc.2016.03.010.

81 C. V. Cushman, P. Brüner, J. Zakel, G. H. Major, B. M. Lunt, N. J. Smith, T. Grehl and M. R. Linford, Low energy ion scattering (LEIS). A practical introduction to its theory, instrumentation, and applications, *Anal. Methods*, 2016, **8**, 3419, DOI: 10.1039/C6AY00765A.

82 G. S. Parkinson and U. Diebold, Adsorption on metal oxide surfaces, in *Surface and Interface Science*, ed. K. Wandelt, John Wiley & Sons, Ltd., 2016, ch. 44, p. 793, DOI: 10.1002/9783527680580.ch44.

83 Vapor pressure calculator, utility by M. Schmid, IAP/TU Wien Surface Physics Group, Vienna, 2018, https://www.iap.tuwien.ac.at/www/surface/vapor_pressure.

84 LEEDpat, Version 4.2, utility by K. E. Hermann (FHI) and M. A. Van Hove (HKBU), Berlin/Hong Kong, 2014, https://www.fhi-berlin.mpg.de/KHsoftware/LEEDpat.

85 J. F. Ziegler, J. P. Biersack and M. D. Ziegler, *SRIM – The Stopping and range of ions in matter*, 2008, http://www.srim.org.

86 P. Lackner, Z. Zou, S. Mayr, U. Diebold and M. Schmid, Using photoelectron spectroscopy to observe oxygen spillover to zirconia, *Phys. Chem. Chem. Phys.*, 2019, **21**, 17613, DOI: 10.1039/c9cp03322j.

87 G. Moretti, Auger parameter and Wagner plot in the characterization of chemical states by X-ray photoelectron spectroscopy: a review, *J. Electron Spectrosc. Relat. Phenom.*, 1998, **95**, 95, DOI: 10.1016/S0368-2048(98)00249-7.

88 J. A. D. Matthew and S. Parker, Correlations between the Auger parameters of oxygen and metal atoms in oxygen-containing compounds, *J. Electron Spectrosc. Relat. Phenom.*, 1997, **85**, 175, DOI: 10.1016/S0368-2048(96)03082-4.

89 F. Hess and B. Yildiz, Polar or not polar? The interplay between reconstruction, Sr enrichment, and reduction at the $La_{0.75}Sr_{0.25}MnO_3(001)$ surface, *Phys. Rev. Mater.*, 2020, **4**, 015801, DOI: 10.1103/PhysRevMaterials.4.015801.

90 D. Halwidl, W. Mayr-Schmölzer, D. Fobes, J. Peng, Z. Mao, M. Schmid, F. Mittendorfer, J. Redinger and U. Diebold, Ordered hydroxyls on $Ca_3Ru_2O_7(001)$, *Nat. Commun.*, 2017, **8**, 23, DOI: 10.1038/s41467-017-00066-w.

91 Z. Wang, A. Loon, A. Subramanian, S. Gerhold, E. McDermott, J. A. Enterkin, M. Hieckel, B. C. Russell, R. J. Green, A. Moewes, J. Guo, P. Blaha, M. R. Castell, U. Diebold and L. D. Marks, Transition from reconstruction toward thin film on the (110) surface of strontium titanate, *Nano Lett.*, 2016, **16**, 2407, DOI: 10.1021/acs.nanolett.5b05211.

92 S. Gerhold, Z. Wang, M. Schmid and U. Diebold, Stoichiometry-driven switching between surface reconstructions on $SrTiO_3(001)$, *Surf. Sci.*, 2014, **621**, L1, DOI: 10.1016/j.susc.2013.10.015.

93 D. S. Mebane, Y. Liu and M. Liu, Refinement of the bulk defect model for $La_xSr_{1-x}MnO_{3\pm\delta}$, *Solid State Ionics*, 2008, **178**, 1950, DOI: 10.1016/j.ssi.2008.01.016.

94 J. Goniakowski, F. Finocchi and C. Noguera, Polarity of oxide surfaces and nanostructures, *Rep. Prog. Phys.*, 2007, **71**, 016501, DOI: 10.1088/0034-4885/71/1/016501.

95 U. Diebold, S.-C. Li and M. Schmid, Oxide surface science, *Annu. Rev. Phys. Chem.*, 2010, **61**, 129, DOI: 10.1146/annurev.physchem.012809.103254.

96 B. C. Russell and M. R. Castell, Reconstructions on the polar $SrTiO_3(110)$ surface: Analysis using STM, LEED, and AES, *Phys. Rev. B*, 2008, **77**, 245414, DOI: 10.1103/PhysRevB.77.245414.

97 M. Niania, R. Podor, T. B. Britton, C. Li, S. J. Cooper, N. Svetkov, S. Skinner and J. Kilner, *In situ* study of strontium segregation in $La_{0.6}Sr_{0.4}Co_{0.2}Fe_{0.8}O_{3-\delta}$ in ambient atmospheres using high-temperature environmental scanning electron microscopy, *J. Mater. Chem. A*, 2018, **6**, 14120, DOI: 10.1039/c8ta01341a.

22960 | *J. Mater. Chem. A*, 2020, **8**, 22947–22961

This journal is © The Royal Society of Chemistry 2020

98 M. Kubicek, G. M. Rupp, S. Huber, A. Penn, A. K. Opitz, J. Bernardi, M. Stöger-Pollach, H. Hutter and J. Fleig, Cation diffusion in La$_{0.6}$Sr$_{0.4}$CoO$_{3-\delta}$ below 800 °C and its relevance for Sr segregation, *Phys. Chem. Chem. Phys.*, 2014, **16**, 2715, DOI: 10.1039/C3CP51906F.

99 B. Koo, H. Kwon, Y. Kim, H. G. Seo, J. W. Han and W. Jung, Enhanced oxygen exchange of perovskite oxide surfaces through strain-driven chemical stabilization, *Energy Environ. Sci.*, 2018, **11**, 71, DOI: 10.1039/c7ee00770a.

100 H. Jalili, J. W. Han, Y. Kuru, Z. Cai and B. Yildiz, New insights into the strain coupling to surface chemistry, electronic structure, and reactivity of La$_{0.7}$Sr$_{0.3}$MnO$_3$, *J. Phys. Chem. Lett.*, 2011, **2**, 801, DOI: 10.1021/jz200160b.

This journal is © The Royal Society of Chemistry 2020

*J. Mater. Chem. A*, 2020, **8**, 22947–22961 | **22961**